

A Lightweight Real-Time Low-Light Enhancement Network for Embedded Automotive Vision Systems

Yuhan Chen^a Yicui Shi^a Guofa Li^{a,*} Guangrui Bai^b Jinyuan Shao^a Xiangfei Huang^a Wenbo Chu^c

Keqiang Li^d

^a College of Mechanical and Vehicle Engineering, Chongqing University, Chongqing 400044, China

^b School of Engineering Science, University of Science and Technology of China, Hefei 230026, China

^c National Innovation Center of Intelligent and Connected Vehicles, Beijing 100089, China

^d School of Vehicle and Mobility, Tsinghua University, Beijing 100084, China

ARTICLE INFO

Keywords:

Image enhancement
Convolutional neural networks
Light weight

ABSTRACT

In low-illumination environments such as nighttime driving, in-vehicle cameras are frequently subject to severe image degradation to challenge driving safety. However, existing low-light image enhancement algorithms are usually with computation intensive network architectures, This limits their practical applications in vehicles. To this end, UltraFast-LieNET is proposed as a lightweight, multi-scale shifted convolutional network for real-time low-light image enhancement. A Dynamic Shifted Convolution kernel (DSConv) is introduced, which consists of only 12 learnable parameters and is primarily designed for efficient feature extraction. By integrating DSConv kernels with multiple shifted distances, a multi-scale shifted residual block (MSRB) is newly constructed to effectively extract multi-scale image features and significantly expand the network's receptive field. To mitigate the instability problem frequently encountered by lightweight networks during gradient propagation, a residual structure is incorporated into UltraFast-LieNET together with a novel multi-level gradient-aware loss function. This approach enhances both the stability of network training and the effectiveness of supervision signals. To accommodate the varying requirements for processing speed across different application scenarios, UltraFast-LieNET allows flexible configuration of both the parameters and the number of DSConv kernels, with the minimum network size comprising only 36 learnable parameters. Experimental results on the LOLI-Street dataset demonstrate that UltraFast-LieNET obtains a PSNR of 26.51 dB, outperforming state-of-the-art methods by 4.6 dB while utilizing only 180 learnable parameters. Across four benchmark datasets, extensive experimental results further validate that UltraFast-LieNET maintains superior capability in balancing real-time performance and image enhancement quality under extremely limited computational resources, indicating strong potential for deployment in practical vehicular systems. Code is available at <https://github.com/YuhanChen2024/UltraFast-LieNET>

1. Introduction

In autonomous and assisted driving systems, low-light images are typically defined as those captured by vehicle-mounted cameras under poorly illuminated conditions, such as at night, in tunnels, or during dawn and dusk. Insufficient ambient lighting and inadequate exposure in these environments lead to color distortion and loss of detail in road surface data, consequently impairing the performance of downstream vision tasks (e.g., detection, recognition, and tracking) and end-to-end autonomous driving systems.

Existing solutions primarily focus on two aspects: hardware and software algorithms. Hardware-based approaches are predominantly targeted at high-end vehicles, where the introduction of costly sensors—including high dynamic range (HDR) sensors, near-infrared (NIR) sensors, and event cameras—significantly enhances visual processing capabilities in low-light conditions [4–6]. However, due to the high cost of hardware and sensors, substantial power

consumption, and limited computational capacity of embedded platforms, these solutions struggle to meet the efficiency and low power consumption requirements of the mass market for intelligent driving systems [7]. Consequently, software-based solutions, primarily relying on low-light image enhancement (LLIE) algorithms, have emerged as the optimal choice to satisfy the needs of most automotive manufacturers.

Early algorithmic studies on low-light driving image enhancement are primarily devoted to traditional image signal processing (ISP) methods, such as global or local histogram equalization and Retinex-based enhancement algorithms [8–12]. Although issues of brightness and contrast are partially alleviated, reliance on manually designed feature extractors and parameter configurations hindered adaptive balancing between detail reconstruction and noise suppression in dynamic, complex driving scenarios, thereby limiting generalization capability. In contrast, deep learning-based enhancement methods have, in recent years, been shown to

* Corresponding author at: College of Mechanical and Vehicle Engineering, Chongqing University, Chongqing 400044, China.

E-mail: liguofa@cqu.edu.cn (G. Li).

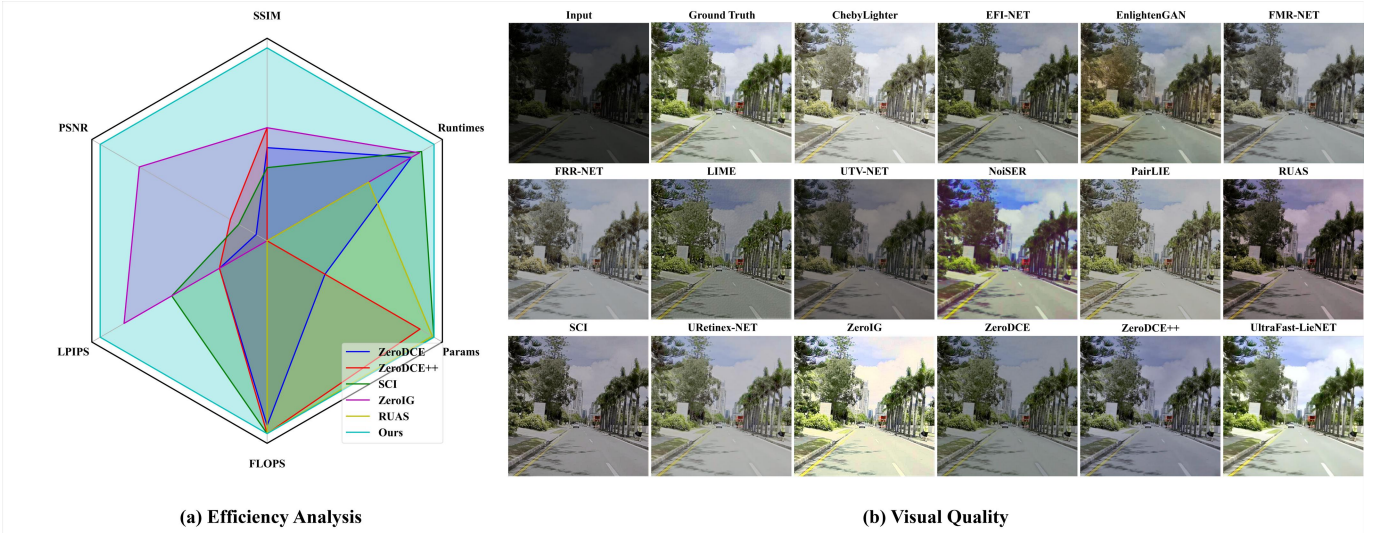


Figure 1. Comparison of performance and efficiency with existing state-of-the-art methods. (a) Image quality metrics (PSNR, SSIM, LPIPS) and computational efficiency (Params, FLOPs, Runtimes).

provide superior scene adaptability and the potential for overall performance improvement through autonomous learning of robust feature representations and nonlinear mappings from large-scale data [13–27].

In the field of low-light image enhancement (LLIE), deep learning methods have primarily followed two paradigms: supervised and unsupervised learning. In supervised learning, illumination mappings are learned from strictly paired low-light and normal-light images, and early network architectures are predominantly based on convolutional neural networks (CNNs) [28–29]. With the evolution of network architecture design, new architectures based on Transformer and Mamba are gradually replacing CNNs as the mainstream solution for supervised learning [30–33]. The core limitation of these methods lies in their strong dependence on paired data, which restricts their generalization ability and scene adaptability. In contrast, unsupervised methods free models from the constraints of paired data. Representative approaches, such as generative adversarial networks (GANs) and diffusion models, enhance generalization and scene adaptability through generative learning mechanisms [13–14, 17, 34–36]. However, deployment efficiency on edge devices is hindered by their large parameter scales, which in turn restricts application flexibility.

Although deep learning has significantly advanced the field of low-light image enhancement (LLIE), current state-of-the-art (SOTA) methods face challenges in achieving an effective balance between computational efficiency and enhancement performance due to high model complexity and deployment constraints. Consequently, efficient real-time inference on in-vehicle embedded platforms remains difficult to achieve. To address the aforementioned challenges, this paper proposes UltraFast-LiNET, an ultra-lightweight network engineered for real-time low-light image enhancement on embedded automotive vision systems. The network incorporates a deeply optimized lightweight backbone architecture specifically tailored for in-vehicle platforms, greatly optimizing memory usage and computational efficiency to support downstream perception tasks. Its performance comparison against SOTA methods is quantitatively illustrated in Figure 1. The core innovations of the network are summarized as follows:

1. A dynamic shift convolution kernel (DSConv) containing merely 12 learnable parameters is proposed in UltraFast-LieNET. Through integration of DSConvs with varying shift distances, a plug-and-play multi-scale shift residual block

(MSRB) is constructed. This module achieves significantly expanded receptive fields with extremely low parameter overhead. Using MSRB as the fundamental building block, an ultra-lightweight backbone network is developed specifically for real-time applications.

2. To enhance the overall learning performance of UltraFast-LieNET, a novel multi-level gradient-aware loss function is introduced to effectively supervise gradient variations of deep features at multiple levels.

3. An ultra-lightweight backbone network is constructed with MSRB as the core component, reducing the parameter count by more than 40% compared with state-of-the-art methods. UltraFast-LieNET simultaneously achieves performance comparable to state-of-the-art approaches on multiple datasets.

2. Related Work

The increasing prevalence of Advanced Driver-Assistance Systems has spurred extensive investigation into lightweight low-light image enhancement algorithms for hardware-constrained platforms such as automotive embedded systems. The lightweight design in this domain primarily focuses on two aspects: the development of lightweight algorithms and the structural optimization of fundamental modules, such as convolution kernels.

2.1 Algorithm lightweight design

In the field of low-light image enhancement, supervised methods are typically built upon backbone networks such as CNN, Transformer, or Mamba, where paired data are directly utilized for supervised learning [28–33]. In contrast, unsupervised methods are mainly developed on architectures such as deconvolutional networks or U-Net, in which illumination transformations are simulated through data generation strategies [13–14, 17, 34–36]. Due to the general-purpose nature of their frameworks, these models usually involve a large number of parameters. In addition, performance improvement often requires the introduction of new branches or structures, which further complicates deployment on vehicular platforms. As a result, lightweight algorithm design has gradually emerged as a central direction. In basic lightweight design, minimal parameter size and computational cost are considered, making it suitable for resource-constrained edge devices. For instance, a lightweight Transformer model with only 90K parameters is proposed by

Cui et al. [37]. Weng et al. combine dark/bright channel priors and gamma correction to achieve low-light enhancement using deep learning, requiring only 25K parameters [38]. Guo et al. frame low-light image enhancement as a task of image-specific curve estimation with deep networks, and proposed ZeroDCE, which enables fast and effective image enhancement with only 10K parameters [13-14]. Ma et al. design a fast, flexible, and robust low-light enhancement framework, SCI, by integrating a cascaded illumination learning process with weight sharing, requiring only 300 learnable parameters [15].

Although basic lightweight design enables significant reduction in parameter count, its effectiveness is often limited in complex scenarios, where challenges such as color distortion, high noise, and detail loss persist. Consequently, lightweight algorithms tailored to specific low-light enhancement scenarios have emerged. For instance, Perez-Zarate et al. propose LoLi-IEA, a two-stage method that first classifies luminance levels and then performs enhancement based on the classification results, focusing on detail extraction and making it suitable for real-time applications [24]. Brateanu et al. optimize color distortion and detail loss with a transformer network based on the YUV color space, achieving superior performance over the Retinex method, and making it suitable for real-time computer vision tasks [39].

The performance of lightweight low-light image enhancement algorithms has been further improved by the integration of recent deep learning techniques, including Transformer, Mamba, and KAN. For instance, Wave-Mamba is proposed by Zou et al., which is based on wavelet domain and state-space models, and enables effective detail recovery as well as accurate color correction [40]. Lu et al. guided by semantic priors, combine the KAN module to enhance high and low-frequency image signals, achieving noise suppression while enhancing the image [41]. Zhang et al. propose STAR, a lightweight Transformer network, suitable for real-time image enhancement, which effectively improves image illumination and corrects white balance [42].

2.2 Basic module structure optimization

Structural optimization of fundamental modules typically prioritizes network pruning and the development of lightweight feature extraction modules, whereas more effective approaches have focused on reconstructing fundamental elements such as convolutional kernels. A primary objective in lightweight architectures is the reduction of kernel parameters while maintaining the receptive field and feature extraction capability. The fundamental paradigm of convolutional kernel lightweighting is primarily achieved through decomposition or grouped convolutions. For example, Xie et al. propose grouped convolutions, which reduce computational overhead by dividing the input channels into multiple groups and performing convolutions independently within each group, thus minimizing cross-channel interactions[43]. Chollet et al. propose the well-known depthwise separable convolution, which decomposes the standard convolution into depthwise convolution (applied independently to each channel) and pointwise convolution (1x1 convolution that fuses channels), significantly reducing computational complexity [44].

Fundamental paradigms are currently widely employed in deep learning architectures. However, they are predominantly concerned with extensive parameter minimization, frequently resulting in compromised accuracy or information redundancy. Consequently, optimization strategies for convolutional kernels aimed at these limitations are being increasingly developed. For instance, Zhang et al. introduce channel

shuffle after grouped convolutions to address the problem of information isolation caused by channel partitioning, thereby enhancing feature interaction while maintaining low computational cost [45]. Sandler et al. design a structure that first expands channels, then applies depthwise convolution, and finally compresses them, which avoids information loss in low-dimensional space and effectively improves accuracy [46]. Han et al. generate "Ghost" feature maps through inexpensive operations to reduce redundant computations, addressing the issue of feature redundancy in depthwise separable convolutions [47]. Huang et al. optimize the grouped structure by learning grouped convolutions to eliminate redundant connections, thereby improving efficiency and mitigating accuracy degradation [48]. The algorithmic performance of lightweight convolutional kernels has been enhanced through the recent introduction of diverse dynamic and optimization mechanisms. These approaches effectively mitigate poor adaptability and unstable optimization in complex scenarios, resulting in substantial gains in both efficiency and robustness. For example, convolutional kernel weights are dynamically adjusted according to the input by Chen et al., addressing the adaptability limitation of static kernels while maintaining lightweight characteristics [49]. Chan et al. employ low-rank decomposition to approximate convolutional kernels, which reduced parameters, mitigated high-dimensional redundancy, and improved computational speed [50]. These advances highlight the effectiveness of lightweight kernel design, although a balance between module performance and computational cost is still required.

3. Proposed Method

As illustrated in Figure 2, a dynamic shifting convolutional kernel (DSConv) with only 12 learnable parameters is presented in this section. Building upon this foundation, a multi-scale shifting residual block (MSRB) is designed and an ultra-lightweight network termed UltraFast-LieNET is constructed for real-time low-light image enhancement, as illustrated in Figure 3. Finally, the various loss functions employed are described, with particular emphasis placed on the newly proposed multi-level gradient-aware loss function.

3.1 Dynamically shifted convolution kernel

To efficiently enlarge the receptive field and capture long-range dependencies without a significant increase in parameters or computational cost, a novel dynamic shifting convolutional kernel (DSConv) is introduced. As illustrated in Figure 2, DSConv expands the receptive field through parallel spatial shifting and feature aggregation, resembling the behavior of dilated convolution while maintaining distinct parameter efficiency and computational structure.

The core idea of DSConv is to replace explicit convolution weight multiplication with an effective combination of spatial shifting and lightweight channel transformations. Drawing inspiration from lightweight algorithms such as FasterNet and GhostNet, DSConv effectively leverages image feature redundancy to further optimize computational efficiency.

Let the input tensor be denoted as $X \in \mathcal{R}^{B \times C \times H \times W}$, where B is the batch size, C is fixed at three channels, H , W denote the height and width of the input features, respectively. The input tensor X is first processed by a pointwise group convolution with a kernel size of 1×1 to produce two independent features for subsequent use, namely the offset feature X_0 , and the residual feature X_r . Information fusion is performed only within each channel. The mathematical formulation is

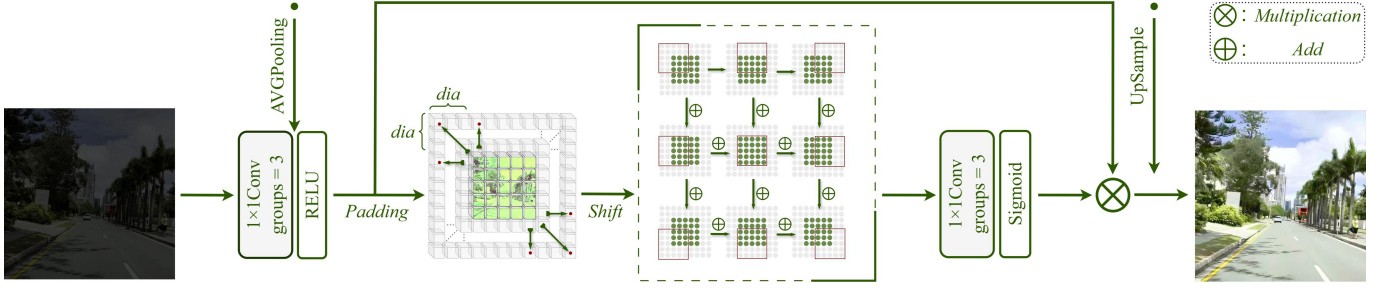


Fig 2. Lightweight architecture of DSConv, including spatial shifting and feature aggregation. Gated modulation is introduced in the output process to enable selective retention and enhancement of aggregated features.

expressed as:

$$X_o = X_r = \text{RELU}(\text{Conv}_{1 \times 1}^{(1)}(X)) \quad (1)$$

where $\text{Conv}_{1 \times 1}^{(1)}$ denotes the first point-wise grouped convolutional layer with kernel size. RELU represents the rectified linear unit activation function. Through this step, $X_o, X_r \in \mathbb{R}^{B \times C \times H \times W}$ is obtained.

To effectively enlarge the receptive field, the offset feature X_0 is used as the basis, and a series of parallel and regular spatial shifting operations are performed to simulate the coverage of convolutional kernels in the spatial dimension. Let the dilation rate of DSConv be denoted as dia . The feature X_0 is first zero-padded, with dia pixels added along the four boundaries (top, bottom, left, and right), resulting in an expanded feature map X_p :

$$X_p = \text{Pad}(X_o, [dia, dia, dia, dia]) \quad (2)$$

At this stage, the dimension of X_p is $X_p \in \mathbb{R}^{B \times C \times (H+2dia) \times (W+2dia)}$. A 3×3 grid sampling is then performed on X_p to generate nine shifted feature maps. Each feature map $X_{i,j}$ is obtained by cropping X_p with a specific offset. Where $i, j \in \{-1, 0, 1\}$ denote the offset indices along the vertical and horizontal directions. For mathematical consistency, the offset is defined as $(i \cdot dia, j \cdot dia)$. At this stage, $X_{i,j}$ is expressed as:

$$X_{i,j} = X_p[:, :, (i+1)dia : (i+1)dia + H, (j+1)dia : (j+1)dia + W] \quad (3)$$

The nine shifted feature maps are summed element-wise and aggregated into a single feature map X_{agg} , This process is expressed as:

$$X_{agg} = \sum_{i \in \{-1, 0, 1\}} \sum_{j \in \{-1, 0, 1\}} X_{i,j} \quad (4)$$

This aggregation process effectively consolidates information from different spatial locations separated by the dilation rate dia . Its effect is equivalent to that of a dilated convolution kernel with a kernel size of 3×3 and a dilation rate of dia .

Finally, to enable the module to adaptively fuse the aggregated information, a gating mechanism is introduced. The aggregated feature X_{agg} is first processed by a second pointwise grouped convolution layer with kernel size of 1×1 , followed by a sigmoid activation function, generating an attention gating map $G \in \mathbb{R}^{B \times C \times H \times W}$. This process is expressed as:

$$G = \text{Sigmoid}(\text{Conv}_{1 \times 1}^{(2)}(X_{agg})) \quad (5)$$

The value range of the gating map G is $(0, 1)$, where a modulation weight is learned for each channel at every spatial location. Finally, the gating map G is multiplied element-wise with the residual feature X_r generated in the first step to obtain the final output Y , which is expressed as:

$$Y = G \otimes X_r \quad (6)$$

This gating mechanism allows the module to dynamically adjust the pathway of the original feature X_r according to the importance of the aggregated information X_{agg} , where

selective retention and enhancement of information are achieved.

Since DSConv is often applied with upsampling or downsampling, average pooling and interpolation-based upsampling are incorporated into its architecture to facilitate network inference.

3.2 Dynamic shift convolution kernel as the basic operator

To demonstrate the efficiency gain of the proposed DSConv, a comparison is conducted with the most functionally similar baseline model, dilated convolution. For parameter comparison, a dilated convolution with a kernel size of 3×3 and a dilation rate of dia is defined as a standard convolution layer to simulate the receptive field expansion achieved by DSConv. As described, the parameter count of DSConv is determined entirely by the weight and bias terms of its two 1×1 pointwise grouped convolutions. In UltraFast-LieNET, the convolutional weights in DSConv are initialized and scaled using the Kaiming Normal method. For a single 1×1 convolutional layer, the weight matrix $W \in \mathbb{R}^{B \times 1 \times 1 \times 1}$ and bias vector $b \in \mathbb{R}^c$ are initialized as follows:

$$W_c \sim \mathcal{N}(0, \sigma^2) \cdot s, \quad b_c = 0 \quad \text{for } c = 1, 2, \dots, C \quad (7)$$

where σ is determined by Kaiming Normal, and $s = 0.1$ denotes the scaling factor. Therefore, the sizes of the weight parameter P_w and the bias parameter P_b in a single convolution layer of DSConv are calculated as follows:

$$P_w = C_{out} \times \frac{C_{in}}{\text{groups}} \times K_H \times K_W = C \times \frac{C}{C} \times 1 \times 1 = C \quad (8)$$

$$P_b = C_{out} = C \quad (9)$$

where K is the convolution kernel size. Therefore, we can quickly deduce that the total number of parameters for a single DSConv is:

$$P_{DSConv} = 2 \times (P_w + P_b) = 4C \quad (10)$$

The total number of parameters of the dilated convolution P_{DSCnv} is expressed as:

$$P_{DSCnv} = P_w + P_b = (C_{out} \times C_{in} \times K_H \times K_W) + C_{out} \quad (11)$$

$$= (C \times C \times 3 \times 3) + C = 9C^2 + C$$

As shown above, the number of parameters of dilated convolution is much higher than that of DSConv. When $C = 256$, the number of parameters of DSConv is about 1/576 of that of dilated convolution.

In terms of computational complexity, DSConv primarily consists of two 1×1 pointwise grouped convolutions, one addition aggregation, and one gated multiplication. The total computational complexity, excluding the activation function, can be expressed as:

$$F_{DSConv} = \underbrace{(4CHW)}_{2 \times \text{Conv}_{1 \times 1}^{(1)}} + \underbrace{(8CHW)}_{\text{Aggregation}} + \underbrace{(2CHW)}_{\text{Conv}_{1 \times 1}^{(2)}} + \underbrace{(CHW)}_{\text{Mul}} = 15CHW \quad (12)$$

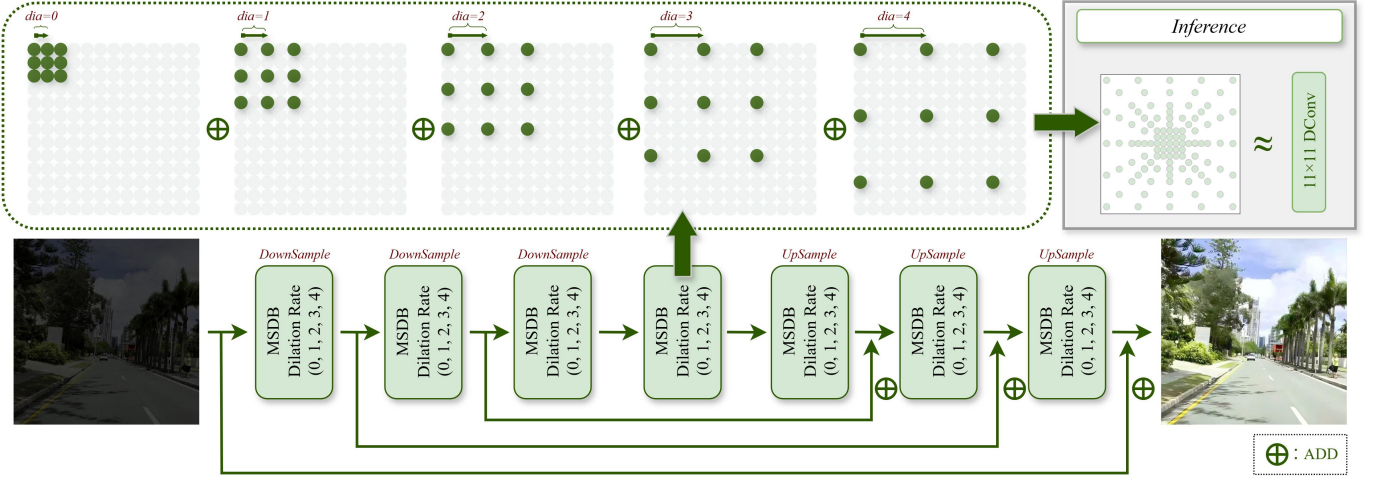


Fig 3. Overall architecture of UltraFast-LieNET. Progressive downsampling and upsampling are performed through multiple MSRBs, and dense skip connections are employed to preserve detailed information.

In contrast, the computational complexity of dilated convolution mainly comes from convolution operation and bias addition. Its total computational complexity F_{DConv} can be expressed as:

$$F_{DConv} = 18C^2HW + CHW \quad (13)$$

From the above analysis, the computational cost of dilated convolution is also much higher than that of DSConv. When $C = 256$, the number of parameters in DSConv is approximately 1/307 of that in dilated convolution, where c denotes the number of channels.

3.3 Network structure

Fig. 3 illustrates the deep auto-encoder architecture of UltraFast-LieNET, which is centered on progressive downsampling and upsampling via multi-scale feature blocks. Dense skip connections are incorporated for detail retention. The network is composed predominantly of plug-and-play multi-scale shifted residual blocks (MSRBs).

The MSRB is the core feature processing module in our design. Its central idea is to integrate multiple DSConvs with different dilation rates in parallel to efficiently capture multi-scale contextual information without introducing additional parameter overhead. A single MSRB consists of κ parallel submodules $\{DSConv_{dia}^{\downarrow}\}_{dia=0}^{\kappa-1}$ ($\kappa = 5$ in this work). Given the input feature $X \in \mathbb{R}^{B \times C \times H \times W}$, the processing of this feature by the module is formulated as:

$$MSRB(X) = \sum_{dia=0}^{\kappa-1} g_{dia}^{\downarrow}(X) = \sum_{dia=0}^{\kappa-1} DSConv_{dia}^{\downarrow}(X) \quad (14)$$

This process indicates that the output of the module is the sum of the outputs from all parallel subpaths. This design enables the network to perceive multiple patterns ranging from fine local features with $dia = 0$ to broader contextual information with $dia = 4$, and its receptive field is equivalent to that of a 11×11 dilated convolution. Based on this scheme, downsampling and upsampling functions are incorporated into DSConv, from which two variants of the MSRB are derived, namely $M^{\downarrow}(X) = \sum_{dia=0}^{\kappa-1} g_{dia}^{\downarrow}(X)$ and $M^{\uparrow}(X) = \sum_{dia=0}^{\kappa-1} g_{dia}^{\uparrow}(X)$. In the upsampling stage, $M^{\uparrow}(X)$ is responsible for upsampling and multi-scale feature fusion, and it also performs the integration of information from skip connections. It receives two inputs: the feature X_{dec} from the previous decoding layer and the skip connection feature X_{enc} from the encoder. The upsampling module is further expressed as:

$$M^{\uparrow}(X) = \sum_{dia=0}^{\kappa-1} g_{dia}^{\uparrow}(X) = \sum_{dia=0}^{\kappa-1} (g_{dia}^{\uparrow}(X_{dec}) \oplus X_{enc}) \quad (15)$$

For a single MSRB, since the five DSConvs are independent, the total number of parameters P_{MSRB} is given as:

$$P_{MSRB} = 5 \times P_{DSConv} = 5 \times 4C = 20C \quad (16)$$

Based on the MSRB, an ultra-lightweight network named UltraFast-LieNET is constructed for real-time low-light image enhancement. Suppose the network contains L processing stages ($L = 3$ in this work), and let l denote the index of different layers ($l = 1, 2, \dots, L$). The encoder is defined as a stack of L $M^{\downarrow}(X)$ blocks, each of which halves the resolution of its input feature map and transforms its representation. The output $X^{(l)}$ of the l -th encoder layer is formulated as:

$$X^{(l)} = M^{\downarrow}(X^{(l-1)}), \text{ for } l = 1, 2, \dots, L \quad (17)$$

where $X^{(0)} = X$ is the original input to the network.

The bottleneck layer consists of only a single MSRB, and its output $X^{(L+1)}$ can be defined as follows:

$$X^{(L+1)} = MSRB(X^{(L)}) \quad (18)$$

The decoder progressively restores the resolution through upsampling blocks and skip connections. The output $O^{(m)}$ of the m -th decoder layer ($m = L, L-1, \dots, 1$) is the sum of the upsampled features and the skip connection features from the $(m-1)$ -th encoder layer, and it is formulated as:

$$O^{(m)} = M^{\uparrow}(O^{(m-1)}, X^{(m-1)}) \oplus X^{(m-1)} \quad (19)$$

Finally, UltraFast-LieNET produces an output for subsequent loss function training supervision. When $\kappa = 5$, UltraFast-LieNET contains only 180 bytes of learnable parameters, with a total computation of 14.036M (denoted as UltraFast-LieNETMax hereafter). When $\kappa = 1$, UltraFast-LieNET contains only 36 bytes of learnable parameters, with a total computation of 2.807M (denoted as UltraFast-LieNETMini hereafter).

3.4 Loss Function

To effectively train UltraFast-LieNET, a composite loss function ℓ_{total} is designed to optimize the quality of the enhanced images from multiple perspectives. This loss function consists of three components: a reconstruction loss ℓ_{rec} , a structural similarity loss $\ell_{ms-ssim}$, and a novel multi-level gradient perception loss ℓ_{grad} . The total loss function ℓ_{total} is defined as the weighted sum of these three components:

$$\ell_{total} = \lambda_{rec}\ell_{rec} + \lambda_{ms-ssim}\ell_{ms-ssim} + \lambda_{grad}\ell_{grad} \quad (20)$$

where λ_{rec} , $\lambda_{ms-ssim}$, λ_{grad} represent the hyperparameters of each loss. Refer to the design concept of L1 and SSIM hybrid loss, λ_{rec} and $\lambda_{ms-ssim}$ are 0.975 and 0.025 respectively[55]. The empirical value of λ_{grad} is 1 (see Table 6 for the ablation experiment of the loss function).

The objective of the reconstruction loss is to minimize the pixel-level difference between the enhanced image and the normal-light image. A smooth L1 loss is adopted as the reconstruction loss function. It combines the advantages of L_1 and L_2 losses, is insensitive to outliers, and provides stable gradients when the error is small. Let the enhanced image be denoted as E and the normal-light image as G . The reconstruction loss ℓ_{rec} is defined as:

$$\ell_{rec}(E, G) = \frac{1}{N} \sum_{i=1}^N \text{smooth}_{L_1}(e_i - g_i) \quad (21)$$

where e_i and g_i represent the i -th pixel value of image E and image G respectively. N is the total pixel value of the image. The smooth_{L_1} function can be defined as follows:

$$\text{smooth}_{L_1}(x) = \begin{cases} 0.5x^2 & \text{if } |x| < 1 \\ |x| - 0.5 & \text{otherwise} \end{cases} \quad (22)$$

Pixel-level loss functions such as L_1 or L_2 are inadequate for capturing structural information consistent with human visual perception. To address this shortcoming, the multi-scale structural similarity (MS-SSIM) index is incorporated as a loss component. This metric assesses perceptual similarity in luminance, contrast, and structure across multiple scales. The MS-SSIM loss is defined as the difference between 1 and the MS-SSIM value, forming a minimization objective expressed as:

$$\ell_{ms-ssim}(E, G) = 1 - MS - SSIM(E, G) \quad (23)$$

The UltraFast-LieNET framework is extremely lightweight, leading to feature degradation during propagation. To mitigate this issue, a multi-level gradient-aware loss function ℓ_{grad} is proposed. This loss enforces gradient consistency constraints across multiple decoder stages, effectively preserving structural information from coarse to fine granularity.

Assume that $\{O_m\}_{m=1}^3$ is the feature map output by the network decoder at three different scales, where O_1 is the final enhanced image E . Therefore, ℓ_{grad} can be expressed as:

$$\ell_{grad} = (\{O_m\}_{m=1}^3, G) = \ell_{rec}(\nabla_y(O_m), \nabla_y(D_k(G))) + \sum_{k=1}^3 \omega_k [\ell_{rec}(\nabla_x(O_m), \nabla_x(D_k(G)))] \quad (24)$$

where ω_k is a hyperparameter that controls the weight of the loss at different scales. Based on the model architecture and experimental validation, $\omega_1 = 1.0$, $\omega_2 = 1.0$, $\omega_3 = 0.04$

are assigned (refer to Figure 6). $D_k(\bullet)$ denotes a downsampling operator that applies bilinear interpolation to adjust the spatial resolution of the input image G to exactly match that of the intermediate feature map O_m . This ensures that gradient comparison is carried out at the same dimensional level. $\nabla_x(\bullet)$ and $\nabla_y(\bullet)$ represent the gradient calculation operations in the horizontal and vertical directions respectively. We use the standard 3×3 Sobel operator to implement it, which is equivalent to convolution with the following convolution kernels K_x and K_y :

$$K_x = \begin{pmatrix} -1 & 0 & 1 \\ -2 & 0 & 2 \\ -1 & 0 & 1 \end{pmatrix}, \quad K_y = \begin{pmatrix} -1 & -2 & -1 \\ 0 & 0 & 0 \\ 1 & 2 & 1 \end{pmatrix} \quad (25)$$

Before applying the operator, all images and feature maps are converted into single-channel grayscale representations so that the loss function focuses on the preservation of luminance gradients.

3.5 Implementation details

The overall architecture of UltraFast-LieNET is implemented using PyTorch and the network is trained using an NVIDIA GeForce RTX 4060 Laptop GPU and a 12th Gen Intel Core i7-12650H processor at 2.30 GHz [56]. Training is conducted for 360 epochs with the Adam optimizer, an initial learning rate of 0.01, and a batch size of 40. The learning rate is multiplied by a decay factor $\gamma = 0.1$ every 40 epochs [57]. The dataset is partitioned into training and testing subsets at a 9:1 ratio. To maintain uniform input dimensions, all training images—including both low-light and normal-light samples—are center-cropped into 180×180 patches. Each patch subsequently undergoes pixel value normalization via the ToTensor operation, which scales integer values to the floating-point interval [0.0, 1.0] and converts the data into PyTorch tensor format.

4. Experiments and Results

The LOL, LSRW-HUAWEI, LSRW-NIKON, and LoLI-Street datasets [58–59, 1] are employed to train and test UltraFast-LieNET. LOL is the first paired dataset designed for supervised low-light image enhancement and is composed of both synthetic and real-world captured data. The LSRW dataset represents the first large-scale real-world paired dataset for low/normal-light images, comprising two distinct subsets acquired using the HUAWEI P40 Pro and NIKON D7500 cameras, respectively. LoLI-Street is the first large-scale low-light image dataset targeting driving scenarios.

Table 1. Performance comparison on the LOL dataset. Red and blue indicate the first and second best results for each metric, respectively.

Method	SSIM↑	PSNR↑	LPIPS↓	NIQE↓	LOE↓	DE↑	EME↑
ZeroDCE++ [13]	0.71	17.32	0.23	3.69	26.74	2.03	17.6
ZeroDCE [14]	0.67	15.67	0.26	3.76	36.6	1.89	17.14
SCI [15]	0.64	15.31	0.23	3.86	6.52	1.97	21.71
RUAS [16]	0.48	12.3	0.27	3.56	1.58	1.48	25.44
EnlightenGAN [17]	0.75	20.13	0.2	3.39	49.08	1.3	3.95
FMR-NET [18]	0.8	23.6	0.27	4.3	51.66	2.14	5.37
LIME [12]	0.61	15.33	0.34	3.78	106.24	1.91	19.28
FRR-NET [19]	0.76	22.11	0.22	3.52	6.23	1.95	8.29
UTV-NET [20]	0.72	16.59	0.23	3.56	21.52	1.78	9.66
ChebyLighter [21]	0.79	22.22	0.17	3.53	16.44	2.1	6.47
EFI-NET [22]	0.67	14.78	0.23	3.55	32.94	1.58	9.59
PairLIE [23]	0.78	21.88	0.23	5.06	64.44	1.88	7.03
NoisER [25]	0.69	19.39	0.47	4.09	88.27	1.83	3.53
URetinex-NET [26]	0.77	23.02	0.21	3.32	18.47	1.99	6.88
ZeroIG [27]	0.63	19.08	0.28	4.59	15.08	2.52	17.71
UltraFast-LieNET _{Max}	0.89	22.57	0.19	3.83	13.9	2.54	19.6

4.1 Comparative LLIE Results

State-of-the-art methods in low-light image enhancement (LLIE) are benchmarked against UltraFast-LieNET. Quantitative results on the LOL, LSRW-HUAWEI, LSRW-NIKON, and LoLI-Street datasets are summarized in Tables

1–4 [1, 12–23, 25–27, 58, 59]. The evaluation employs full-reference metrics (PSNR, SSIM, LPIPS) and no-reference metrics (NIQE, LOE, DE, EME). Top-two results in PSNR and SSIM are attained across all datasets except Table 2. Similarly, excellent rankings are achieved across all remaining metrics.

Table 2. Performance comparison on the LSRW-HUAWEI dataset. Red and blue indicate the first and second best results for each metric, respectively.

Method	SSIM↑	PSNR↑	LPIPS↓	NIQE↓	LOE↓	DE↑	EME↑
ZeroDCE++ [13]	0.24	12.88	0.38	3.5	9.94	2.4	37.17
ZeroDCE [14]	0.22	12.33	0.37	3.81	8.36	2.27	37.71
SCI [15]	0.17	11.57	0.44	4.12	2.19	1.9	38.63
RUAS [16]	0.12	10.66	0.54	5.04	1.9	1.17	43.7
EnlightenGAN [17]	0.36	16.45	0.42	3.75	62.62	1.92	2.17
FMR-NET [18]	0.45	20.22	0.39	3.97	41.25	3.01	4.49
LIME [12]	0.17	12.6	0.47	4.89	130.84	2.76	42.71
FRR-NET [19]	0.37	17.83	0.3	3.77	3.21	2.76	7.4
UTV-NET [20]	0.33	14.48	0.35	3.05	15.84	2.67	9.52
ChebyLighter [21]	0.37	14.32	0.39	3.06	46.86	2.98	7.08
EFI-NET[22]	0.27	12.16	0.43	3.49	16.47	1.91	7.99
PairLIE [23]	0.41	15.91	0.42	4.32	42.15	2.51	5.4
NoisER [25]	0.34	14.73	0.61	5.38	85.02	1.39	1.34
URetinex-NET [26]	0.37	17.67	0.35	2.85	19.47	3.2	11
ZeroIG[27]	0.26	14.07	0.35	4.65	5.7	2.42	38.02
UltraFast-LieNET _{Max}	0.52	16.93	0.32	3.52	9.54	3.7	16.05

Table 3. Performance comparison on the LSRW-NIKON dataset. Red and blue indicate the first and second best results for each metric, respectively.

Method	SSIM↑	PSNR↑	LPIPS↓	NIQE↓	LOE↓	DE↑	EME↑
ZeroDCE++ [13]	0.22	14.12	0.28	2.62	29.26	1.74	8.79
ZeroDCE [14]	0.22	13.58	0.29	2.85	70.83	1.52	8.87
SCI [15]	0.2	13.18	0.32	2.73	15.01	1.76	10.76
RUAS [16]	0.18	11.15	0.35	2.62	0.57	1.45	11.65
EnlightenGAN [17]	0.29	15.79	0.38	3.09	97.7	0.33	1.96
FMR-NET [18]	0.25	15.51	0.31	2.99	32.85	1.77	4.54
LIME [12]	0.17	12.83	0.35	3.38	97.35	1.63	11.1
FRR-NET [19]	0.25	15.9	0.3	2.66	15.18	1.54	5.55
UTV-NET [20]	0.24	12.51	0.32	3.22	19.21	1.22	6.62
ChebyLighter [21]	0.24	14.83	0.3	2.73	37.5	1.65	4.49
EFI-NET[22]	0.21	12.69	0.29	2.42	46.72	1.44	7.56
PairLIE [23]	0.22	15.52	0.27	3.68	75	1.59	5.53
NoisER [25]	0.26	15.49	0.43	3.77	78.71	1.55	3.27
URetinex-NET [26]	0.24	15.89	0.26	2.32	35.28	1.62	4.6
ZeroIG[27]	0.17	13.37	0.34	2.83	19.93	2.12	9.42
UltraFast-LieNET _{Max}	0.32	17.46	0.32	2.39	31.04	1.79	9.44

Table 4. Performance comparison on the LoLI-Street dataset. Red and blue indicate the first and second best results for each metric, respectively.

Method	SSIM↑	PSNR↑	LPIPS↓	NIQE↓	LOE↓	DE↑	EME↑
ZeroDCE++ [13]	0.87	13.87	0.23	3.48	60.09	0.84	4.09
ZeroDCE [14]	0.84	13.31	0.22	3.29	68.16	0.23	3.94
SCI [15]	0.86	14.93	0.21	3.09	24.03	1.06	5.26
RUAS [16]	0.81	12.43	0.24	3.21	0.05	1.36	6.26
EnlightenGAN [17]	0.9	17.18	0.15	3.17	98.38	1.21	2.71
FMR-NET [18]	0.85	13.77	0.23	3.94	5.1	0.92	2.12
LIME [12]	0.74	11.54	0.36	3.31	151.06	0.98	5.35
FRR-NET [19]	0.87	14.77	0.2	3.58	7.56	0.72	2.32
UTV-NET [20]	0.74	9.54	0.28	3.75	26.16	0.74	3.39
ChebyLighter [21]	0.91	20.91	0.12	3.11	6.61	1.19	2.02
EFI-NET[22]	0.86	13.72	0.18	3.14	27.36	1.09	3.07
PairLIE [23]	0.88	18.3	0.19	3.45	105.06	0.72	2.26
NoisER [25]	0.77	14.32	0.44	4.41	53.22	1.38	2.53
URetinex-NET [26]	0.89	18.56	0.14	3.97	26.02	0.69	2.29
ZeroIG[27]	0.82	17.5	0.22	3.19	36	1.32	4.4
UltraFast-LieNET _{Max}	0.92	19.27	0.13	3.42	30.51	1.58	2.73

Table 5. Computational efficiency comparison on the LOL dataset. Red and blue indicate the first and second best results for each metric, respectively.

Method	SSIM \uparrow	PSNR \uparrow	Params (KB) \downarrow	FLOPs (G) \downarrow	Runtimes (ms) \downarrow
ZeroDCE++ [13]	0.7	14.27	10.6	0.33	3.99
ZeroDCE [14]	0.66	13.08	79.4	5.21	7.03
SCI [15]	0.63	13.9	0.3	0.0619	1.98
RUAS [16]	0.51	12.59	1.4	0.2813	10.1
EnlightenGAN [17]	0.84	17.22	8636	61.01	10.6
FMR-NET [18]	0.84	23.82	196.8	102.8	116
LIME [12]	0.57	12.19	N/A	N/A	758
FRR-NET [19]	0.82	17.21	12.21	0.216	75.7
UTV-NET [20]	0.68	13.85	7745	58.29	46.5
ChebyLighter [21]	0.84	24.01	73	17.25	76.4
EFI-NET [22]	0.66	13.18	129.2	9.38	44.8
PairLIE [23]	0.81	16.96	34.18	22.35	28.4
NoisER [25]	0.72	19.33	1.763	8.62	3.02
URetinex-NET [26]	0.8	19.46	838.3	136.01	36.9
ZeroIG [27]	0.69	18.58	123.63	118.73	17.2
UltraFast-LieNET _{Mini}	0.78	21.63	0.036	0.000003	1.72
UltraFast-LieNET _{Max}	0.86	24.98	0.18	0.000014	2.69

To evaluate the computational efficiency of UltraFast-LieNET, both the proposed method and state-of-the-art approaches are deployed on a Jetson AGX Orin 64GB platform. The device features an NVIDIA Ampere architecture GPU with 2048 CUDA cores and 64 Tensor Cores, accompanied by a 12-core Arm Cortex-A78AE v8.2 64-bit CPU. The parameter counts and computational efficiency of UltraFast-LieNET and comparative methods are presented in Table 5. Runtime measurements are obtained using 600 \times 400 images from the LOL dataset, averaged over 10 executions. The proposed method demonstrates leading performance across all metrics. Considering that the model size of UltraFast-LieNET is significantly smaller than that of state-of-the-art methods, the evaluation results presented above are remarkable.

Fig. 4-7 display the visual comparisons of images selected from the LOL, LSRW-HUAWEI, LSRW-NIKON, and LoLI-

Street datasets. Effective color restoration is observed in all examples. In the Fig. 4, UltraFast-LieNET demonstrates superior performance in recovering brightness and color. While saturation is reduced compared to ZeroIG, the result more accurately approximates the reference image. The Fig. 5 demonstrates more balanced global image processing by UltraFast-LieNET, avoiding the uneven brightness characteristic of EnlightenGAN. Although PairLIE and ZeroIG yield higher saturation and improved denoising performance, the proposed method provides results closer to the reference image. This is confirmed in the Fig. 6. Excessive brightness in ZeroIG's output results in substantial loss of detail in clouds and haze, whereas the proposed method effectively preserves these details. The Fig. 7 demonstrates the absence of banding artifacts in the proposed method's results under extremely low-light conditions.

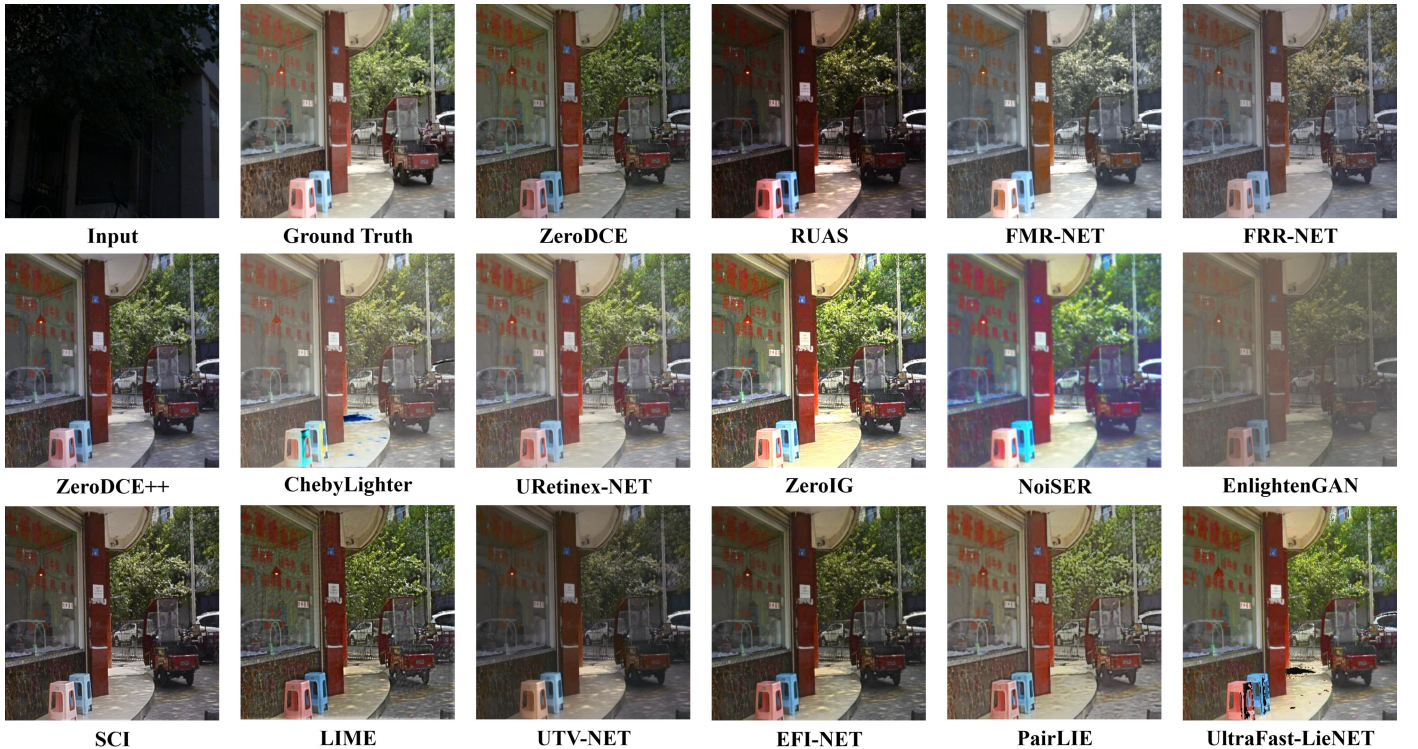


Fig 4. Visual comparison of UltraFast-LieNET and SOTA methods on the LSRW-HUAWEI dataset.

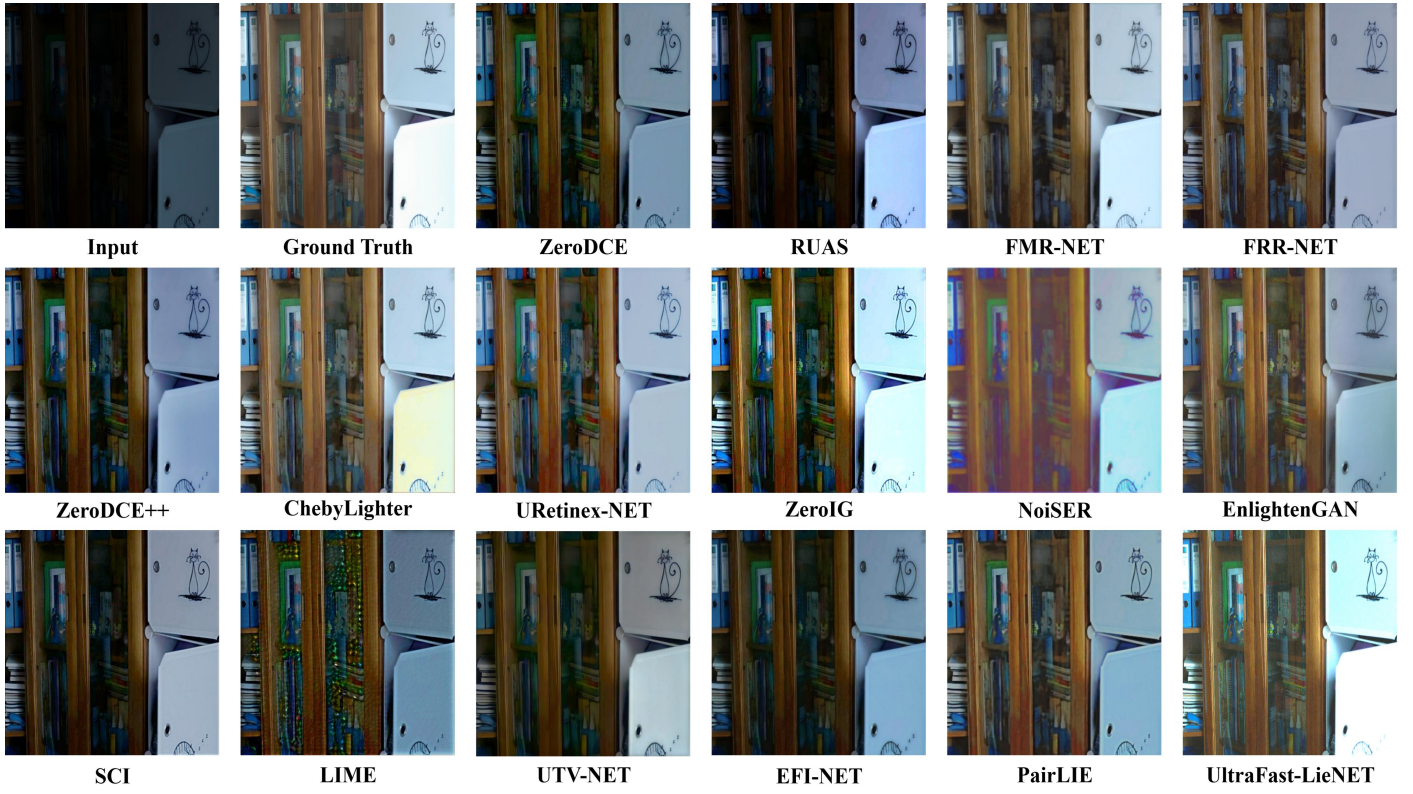


Fig 5. Visual comparison of UltraFast-LieNET and SOTA methods on the LoLI-Street dataset.

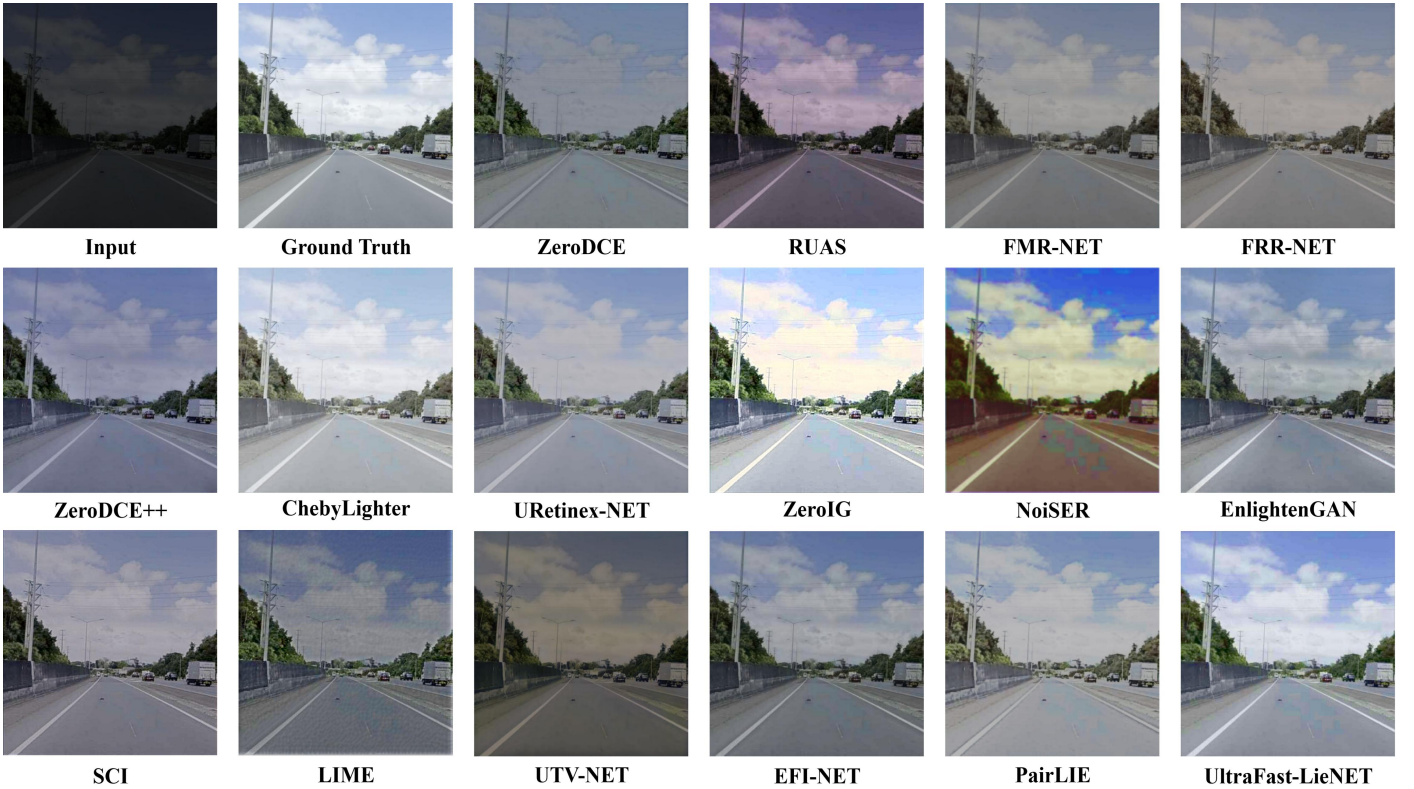


Fig 6. Visual comparison of UltraFast-LieNET and SOTA methods on the LOL dataset.

Fig. 8 presents an evaluation of UltraFast-LieNET's detail restoration capability using complex scenes from the LOL dataset. The method demonstrates state-of-the-art detail reconstruction despite slightly higher saturation relative to the reference image. Common artifacts including low brightness, color distortion, and over-sharpening are effectively avoided.

In conclusion, while UltraFast-LieNET demonstrates some generalization limitations in enhancing certain images, its performance is notable given a maximum of 180 learnable parameters. The method effectively balances image quality with computational efficiency and achieves superior performance compared to state-of-the-art approaches.

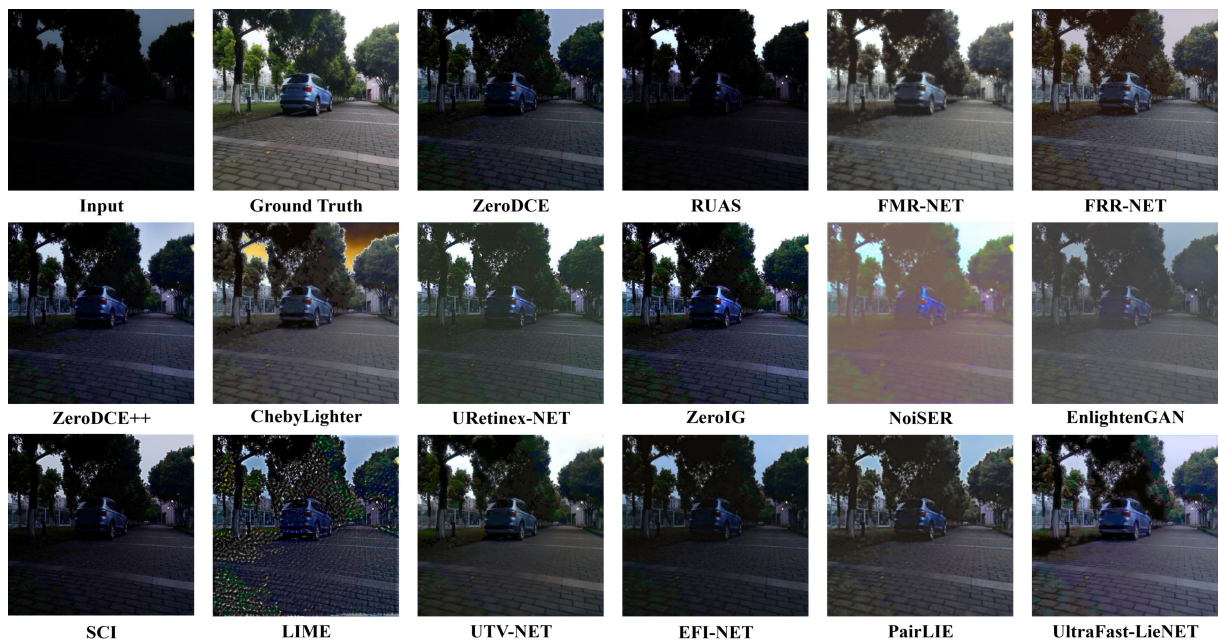


Fig 7. Visual comparison of UltraFast-LieNET and SOTA methods on the LSRW-NIKON dataset.



Fig 8. Comparison of detailed features between UltraFast-LieNET and SOTA methods on the LOL dataset. The second image of each method is a magnified image of the details in the red box.

4.2 Ablation Study

Ablation studies on the LOL dataset evaluate the effectiveness of the loss function selection, the appropriateness of parameter settings in the multi-level gradient-aware loss function ℓ_{grad} , and the influence of varying quantities and *dia* configurations of DSconv blocks. The effectiveness of loss function selection is investigated in Table 6. The composite loss function ℓ_{total} achieves the best performance. Additionally, the results confirm that ℓ_{grad} improves the SSIM metric effectively.

Table 6. Ablation study on loss function selection conducted on the LOL dataset.

Smooth L1	MS-SSIM	Grad	PSNR↑	SSIM↑
√	√	√	24.98	0.86
√	√	×	19.71	0.75
×	×	√	17.53	0.77
√	×	×	18.46	0.69
√	×	√	18.91	0.82
×	√	√	17.89	0.71
×	√	×	17.38	0.71

Fig. 9 presents an ablation study on the parameter configuration of the multi-level gradient-aware loss function ℓ_{grad} . The hyperparameters ω_k providing optimal PSNR performance in UltraFast-LieNET are identified. Experimental results confirm that proper hyperparameter selection contributes to the method's effectiveness.

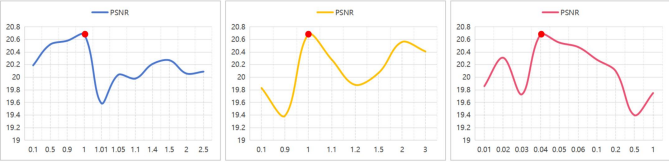


Fig 9. Ablation study on the correctness of hyperparameters in the multi-level gradient-aware loss function conducted on the LOL dataset.

An ablation study evaluates the impact of varying quantities and dilation settings of DSconv blocks using the LoLI-Street dataset. Table 7 presents PSNR and SSIM values obtained with DSconv configurations and rates. Specifically, the notation 2+3+4 denotes the following MSRB combination:

$$MSRB(X) = \sum_{dia=2}^4 g_{dia}(X) = \sum_{dia=2}^4 DSconv_{dia}(X) \quad (26)$$

It is evident that the best performance is achieved when UltraFast-LieNET combines more DSConv layers. To minimize the model's parameter size, no further fusion of additional DSConv layers is performed in this work.

5. Conclusion

This paper presents UltraFast-LiNET, an ultra-lightweight convolutional network designed for real-time low-light image enhancement in embedded automotive vision systems. To meet the stringent computational and latency constraints of in-vehicle platforms, the network is engineered with extreme parameter efficiency, requiring only 180 learnable parameters—and as few as 36 in its most compact form. Extensive experiments confirm that UltraFast-LiNET achieves state-of-the-art enhancement quality while operating in real-time, making it particularly suitable for deployment on resource-limited automotive hardware. Future work will focus on further optimizing inference speed, enhancing robustness to diverse and extreme driving conditions, and integrating the model into full-scale embedded vision pipelines for autonomous driving applications.

Table 7. Ablation study on the impact of different numbers and *dia* settings of DSConv on the model using the LoLI-Street dataset.

<i>dia</i>	PSNR↑	SSIM↑
0	21.45	0.71
0+1	22.43	0.74
0+1+2	22.73	0.74
0+1+2+3	23.41	0.81
0+1+2+3+4	24.76	0.89
1	17.8	0.61
1+2	18.2	0.73
1+2+3	23.63	0.78
1+2+3+4	23.72	0.87
2	16.23	0.59
2+3	23	0.8
2+3+4	24.02	0.86
3	17.22	0.67
3+4	18.09	0.74
4	15.1	0.62

CRediT authorship contribution statement

Yuhan Chen: Conceptualization, Methodology, Visualization, Writing - original draft, Writing - review & editing, Resources, Formal analysis, Software, Validation. **Yicui Shi:** Data curation, Investigation, Software, Writing - review & editing. **Guofa Li:** Methodology, Funding acquisition, Supervision, Resources, Writing - review & editing. **Guangrui Bai:** Methodology, Writing - review & editing. **Jinyuan Shao:** Software, Writing - review & editing. **Xiangfei Huang:** Visualization, Writing - review & editing. **Wenbo Chu:** Resources, Writing - review & editing. **Keqiang Li:** Resources, Writing - review & editing.

Declaration of Competing Interest

The authors declare that they have no known competing financial interests or personal relationships that could have appeared to influence the work reported in this paper.

Data availability

The authors do not have permission to share data.

References

- [1] Md. Tanvir. Islam, Inzamamul. Alam, Simon. S. Woo, Saeed. Anwar, IK. Hyun. Lee, Khan. Muhammad, “Loli-street: Benchmarking low-light image enhancement and beyond,” Proceedings of the Asian Conference on Computer Vision (ACCV), 2024, pp. 1250-1267.
- [2] Li. C, Guo. C, Han. L et al., “Low-light image and video enhancement using deep learning: A survey,” IEEE transactions on pattern analysis and machine intelligence, vol. 44, no. 12, pp. 9396-9416, 2022.
- [3] Zhao. Q, Li. G, He. B et al., “Deep Learning for Low-Light Vision: A Comprehensive Survey,” IEEE Transactions on Neural Networks and Learning Systems, 2025.
- [4] Bai. G, Yan. H, Liu. W et al., “Towards Lightest Low-Light Image Enhancement Architecture for Mobile Devices,” Expert Systems with Applications, vol. 296, p. 129125, 2026.
- [5] Z. Guo, S. Perminov, M. Konenkov and D. Tsetserukou, “HawkDrive: A Transformer-driven Visual Perception System for Autonomous Driving in Night Scene,” 2024 IEEE Intelligent Vehicles Symposium (IV), 2024, pp. 2598-2603.
- [6] Liu. X, Wu. Z, Li. A et al., “NTIRE 2024 challenge on low light image enhancement: Methods and results,” Proceedings of the IEEE/CVF Conference on Computer Vision and Pattern Recognition (CVPR), 2024, pp. 6571-6594.
- [7] Ozcan. M, Ergezer. H, Ayazoğlu. M, “FLIGHT mode on: A feather-

- light network for low-light image enhancement,” *Proceedings of the IEEE/CVF Conference on Computer Vision and Pattern Recognition (CVPR)*, 2023, pp. 4226-4235.
- [8] Pisano. E. D, Zong. S, Hemminger. B. M et al., “Contrast limited adaptive histogram equalization image processing to improve the detection of simulated spiculations in dense mammograms,” *Journal of Digital imaging*, vol. 11, no. 4, p. 193, 1998.
 - [9] Abdullah-Al-Wadud. M, Kabir. M. H, Dewan. M. A. A et al., “A dynamic histogram equalization for image contrast enhancement,” *IEEE Transactions on Consumer Electronics*, vol. 53, no. 2, pp. 593-600, 2007.
 - [10] Pizer. S. M, Amburn. E. P, Austin. J. D et al., “Adaptive histogram equalization and its variations,” *Computer Vision, Graphics, and Image Processing*, vol. 39, no. 3, pp. 355-368, 1987.
 - [11] Land. E. H, McCann. J. J, “Lightness and retinex theory,” *Journal of the Optical Society of America*, vol. 61, no. 1, pp. 1-11, 1971.
 - [12] Guo. X, Li. Y, Ling. H, “LIME: low-light image enhancement via illumination map estimation,” *IEEE Transactions on Image Processing*, vol. 26, no. 2, pp. 982-993, 2017.
 - [13] Li. C, Guo. C, Loy. C. C, “Learning to enhance low-light image via zero-reference deep curve estimation,” *IEEE Transactions on Pattern Analysis and Machine Intelligence*, vol. 44, no. 8, pp. 4225-4238, 2022.
 - [14] Guo. C, Li. C, Guo. J et al., “Zero-reference deep curve estimation for low-light image enhancement,” *Proceedings of the IEEE/CVF Conference on Computer Vision and Pattern Recognition (CVPR)*, 2020, pp. 1780-1789.
 - [15] Ma. L, Ma. T, Liu. R et al., “Toward fast, flexible, and robust low-light image enhancement,” *Proceedings of the IEEE/CVF Conference on Computer Vision and Pattern Recognition (CVPR)*, 2022, pp. 5637-5646.
 - [16] Liu. R, Ma. L, Zhang. J et al., “Retinex-inspired unrolling with cooperative prior architecture search for low-light image enhancement,” *Proceedings of the IEEE/CVF Conference on Computer Vision and Pattern Recognition (CVPR)*, 2021, pp. 10561-10570.
 - [17] Jiang. Y et al., “EnlightenGAN: deep light enhancement without paired supervision,” *IEEE Transactions on Image Processing*, vol. 30, pp. 2340-2349, 2021.
 - [18] Chen. Y, Zhu. G, Wang. X et al., “FMR-Net: a fast multi-scale residual network for low-light image enhancement,” *Multimedia Systems*, vol. 30, p. 73, 2024.
 - [19] Chen. Y, Zhu. G, Wang. X et al., “FRR-NET: a fast reparameterized residual network for low-light image enhancement,” *Signal, Image and Video Processing*, vol. 18, pp. 4925 – 4934, 2024.
 - [20] Zheng. C, Shi. D, Shi. W, “Adaptive unfolding total variation network for low-light image enhancement,” *Proceedings of the IEEE/CVF International Conference on Computer Vision (ICCV)*, 2021, pp. 4439-4448.
 - [21] Pan. J, Zhai. D, Bai. Y et al., “ChebyLighter: optimal curve estimation for low-light image enhancement,” *Proceedings of the 30th ACM International Conference on Multimedia*, pp. 1358 – 1366, 2022.
 - [22] Liu. C, Wu. F, Wang. X, “EFINet: restoration for low-light images via enhancement-fusion iterative network,” *IEEE Transactions on Circuits and Systems for Video Technology*, vol. 32, no. 12, pp. 8486-8499, 2022.
 - [23] Fu. Z, Yang. Y, Tu. X et al., “Learning a simple low-light image enhancer from paired low-light instances,” *Proceedings of the IEEE/CVF Conference on Computer Vision and Pattern Recognition (CVPR)*, 2023, pp. 22252-22261.
 - [24] Perez-Zarate. E, Ramos-Soto. O, Rodriguez-Esparza. E et al., “LoLi-IEA: low-light image enhancement algorithm,” *Applications of Machine Learning 2023*, vol. 12675, pp. 248-263, 2023.
 - [25] Zhang. Z et al., “Noise self-regression: a new learning paradigm to enhance low-light images without task-related data,” *IEEE Transactions on Pattern Analysis and Machine Intelligence*, vol. 47, no. 2, pp. 1073 – 1088, 2025.
 - [26] Wu. W, Weng. J, Zhang. P et al., “Uretinex-net: Retinex-based deep unfolding network for low-light image enhancement,” *Proceedings of the IEEE/CVF Conference on Computer Vision and Pattern Recognition (CVPR)*, 2022, pp. 5901-5910.
 - [27] Shi. Y, Liu. D, Zhang. L et al., “ZERO-IG: Zero-shot illumination-guided joint denoising and adaptive enhancement for low-light images,” *Proceedings of the IEEE/CVF Conference on Computer Vision and Pattern Recognition (CVPR)*, 2024, pp. 3015-3024.
 - [28] Lore. K. G, Akintayo. A, Sarkar. S, “LLNet: a deep autoencoder approach to natural low-light image enhancement,” *Pattern Recognition*, vol. 61, pp. 650 – 662, 2017.
 - [29] C. Wei, W. Wang, W. Yang, and J. Liu, “Deep Retinex Decomposition for Low-Light Enhancement,” *arXiv preprint arXiv: 1808.04560*.
 - [30] Jiang. N, Lin. J, Zhang. T et al., “Low-light image enhancement via stage-transformer-guided network,” *IEEE Transactions on Circuits and Systems for Video Technology*, vol. 33, no. 8, pp. 3701 – 3712, 2023.
 - [31] Wen. Y, Xu. P, Li. Z et al., “An illumination-guided dual attention vision transformer for low-light image enhancement,” *Pattern Recognition*, vol. 158, p. 111033, 2025.
 - [32] Bai. J, Yin. Y, He. Q et al., “Retinexmamba: retinex-based mamba for low-light image enhancement,” *International Conference on Neural Information Processing*, pp. 427 – 442, 2024.
 - [33] Chen. X, Han. L, Huang. P et al., “Retinex-RAWMamba: bridging demosaicing and denoising for low-light RAW image enhancement,” *IEEE Transactions on Circuits and Systems for Video Technology*, 2025.
 - [34] Ghosh. S, Hua. Y, Mukherjee. S. S et al., “IEGAN: multi-purpose perceptual quality image enhancement using generative adversarial network,” *2019 IEEE Winter Conference on Applications of Computer Vision (WACV)*, 2019, pp. 11 – 20.
 - [35] Du. D, Li. E, Si. L et al., “UIEDP: boosting underwater image enhancement with diffusion prior,” *Expert Systems with Applications*, vol. 259, p. 125271, 2025.
 - [36] Wang. T, Zhang. K, Zhang. Y et al., “LLDiffusion: learning degradation representations in diffusion models for low-light image enhancement,” *Pattern Recognition*, vol. 166, p. 111628, 2025.
 - [37] Cui. Z, Li. K, Gu. L et al., “You only need 90k parameters to adapt light: a light weight transformer for image enhancement and exposure correction,” *arXiv preprint arXiv: 2205.14871*.
 - [38] Weng. S. E, Miaou. S. G, Christanto. R, “A lightweight low-light image enhancement network via channel prior and gamma correction,” *arXiv preprint arXiv: 2402.18147*.
 - [39] Brateanu. A, Balmez. R, Avram. A et al., “LYT-NET: lightweight YUV transformer-based network for low-light image enhancement,” *IEEE Signal Processing Letters*, vol. 32, pp. 2065 – 2069, 2025.
 - [40] Zou. W, Gao. H, Yang. W et al., “Wave-mamba: Wavelet state space model for ultra-high-definition low-light image enhancement,” *Proceedings of the 32nd ACM International Conference on Multimedia*, 2024, pp. 1534-1543.
 - [41] Lu. C, Wei. Z, Wu. H, et al., “KANformer: Dual-priors-guided low-light enhancement via KAN and Transformer,” *ACM Transactions on Multimedia Computing, Communications and Applications*, 2025.
 - [42] Zhang. Z, Jiang. Y, Jiang. J et al., “Star: A structure-aware lightweight transformer for real-time image enhancement,” *Proceedings of the IEEE/CVF International Conference on Computer Vision (ICCV)*, 2021, pp. 4106-4115.
 - [43] Xie. S, Girshick. R, Dollár. P et al., “Aggregated residual transformations for deep neural networks,” *Proceedings of the IEEE Conference on Computer Vision and Pattern Recognition (CVPR)*, 2017, pp. 1492-1500.
 - [44] Chollet. F, “Xception: Deep learning with depthwise separable convolutions,” *Proceedings of the IEEE Conference on Computer Vision and Pattern Recognition (CVPR)*, 2017, pp. 1251-1258.
 - [45] Zhang. X, Zhou. X, Lin. M et al., “Shufflenet: An extremely efficient convolutional neural network for mobile devices,” *Proceedings of the IEEE Conference on Computer Vision and Pattern Recognition (CVPR)*, 2018, pp. 6848-6856.
 - [46] Sandler. M, Howard. A, Zhu. M et al., “Mobilenetv2: Inverted residuals and linear bottlenecks,” *Proceedings of the IEEE Conference on Computer Vision and Pattern Recognition (CVPR)*, 2018, pp. 4510-4520.
 - [47] Han. K, Wang. Y, Tian. Q et al., “Ghostnet: More features from cheap

- operations,” Proceedings of the IEEE/CVF Conference on Computer Vision and Pattern Recognition (CVPR), 2020, pp. 1580-1589.
- [48] Huang. G, Liu. S, Van der Maaten. L et al., “Condensenet: An efficient densenet using learned group convolutions,” Proceedings of the IEEE Conference on Computer Vision and Pattern Recognition (CVPR), 2018, pp. 2752-2761.
- [49] Chen. Y, Dai. X, Liu. M et al., “Dynamic convolution: Attention over convolution kernels,” Proceedings of the IEEE/CVF Conference on Computer Vision and Pattern Recognition (CVPR), 2020, pp. 11030-11039.
- [50] Chan. T, Jia. K, Gao. S et al., “PCANet: A Simple Deep Learning Baseline for Image Classification?,” IEEE Transactions on Image Processing, vol. 24, no. 12, pp. 5017-5032, 2015.
- [51] Wu. B, Wan. A, Yue. X et al., “Shift: A zero flop, zero parameter alternative to spatial convolutions,” Proceedings of the IEEE Conference on Computer Vision and Pattern Recognition (CVPR), 2018, pp. 9127-9135.
- [52] Yu. F, Koltun. V, “Multi-scale context aggregation by dilated convolutions,” arXiv preprint arXiv: 1511.07122.
- [53] Qin. D, Leichner. C, Delakis. M et al., “MobileNetV4: Universal models for the mobile ecosystem,” Proceedings of the European Conference on Computer Vision (ECCV), 2024, pp. 78-96.
- [54] Chen. J, Kao. S, He. H et al., “Run, don't walk: chasing higher FLOPS for faster neural networks,” Proceedings of the IEEE/CVF Conference on Computer Vision and Pattern Recognition (CVPR), 2023, pp. 12021-12031.
- [55] Zhao. H, Gallo. O, Frosio. I et al., “Loss functions for neural networks for image processing,” arXiv preprint arXiv: 1511.08861.
- [56] Paszke. A, Gross. S, Massa. F et al., “Pytorch: An imperative style, high-performance deep learning library,” Advances in Neural Information Processing Systems, vol. 32, pp. 8024-8035, 2019.
- [57] Kinga. D, Adam. J, “A method for stochastic optimization,” Proceedings of the International Conference on Learning Representations (ICLR), 2015, pp. 5-6.
- [58] Wei. C, Wang. W, Yang. W et al., “Deep retinex decomposition for low-light enhancement,” arXiv preprint arXiv: 1808.04560.
- [59] Hai. J, Xuan. Z, Yang. R et al., “R2rnet: Low-light image enhancement via real-low to real-normal network,” Journal of Visual Communication and Image Representation, vol. 90, p. 103712, 2023.